



The color dipole picture of low-x DIS

Dieter Schildknecht

Fakultät für Physik, Universität Bielefeld, Universitätsstraße 25, 33615 Bielefeld, Germany
and

Max-Planck-Institute for Physics, Föhringer Ring 6, 80805 Munich, Germany
E-Mail: Dieter.Schildknecht@physik.uni-bielefeld.de

Abstract

Deep inelastic electron scattering (DIS) from nucleons at low values of the Bjorken variable $x \cong Q^2/W^2 \lesssim 0.1$ proceeds via fluctuations of the photon into quark-antiquark dipole states that subsequently interact with the gluon field in the nucleon. Dependent on the interaction energy, W , the color-gauge-invariant dipole interaction with the gluon field in the nucleon, for any fixed dipole size, contains the limits of i) color transparency and ii) saturation, where “saturation” stands for the approach to a hadronlike dipole-proton interaction cross section. All essential features of the experimental results on low-x DIS, as a consequence of the color-gauge-invariant dipole interaction follow model independently i.e. without specific ansatz for the dipole cross section. The model-independent results in particular include the low-x scaling behavior of the photoabsorption cross section, $\sigma_{\gamma^* p}(W^2, Q^2) = \sigma_{\gamma^* p}(\eta(W^2, Q^2))$, with definite functional dependence on the low-x scaling variable $\eta(W^2, Q^2) \cong Q^2/\Lambda_{sat}^2(W^2)$ in the limits of $\eta(W^2, Q^2) \gg 1$ and $\eta(W^2, Q^2) \ll 1$, respectively. Consistency with the pQCD-improved parton model implies the definite value of $C_2 \cong 0.29$ for the exponent in the “saturation scale”, $\Lambda_{sat}^2(W^2) \approx (W^2)^{C_2}$. The longitudinal-to-transverse ratio of the photoabsorption cross section at large Q^2 has the definite value of $R = 1/2\rho$ with $\rho = 4/3$. For $W^2 \rightarrow \infty$ at any fixed Q^2 , the photoabsorption cross section converges towards a Q^2 -independent saturation limit that coincides with the cross section for $Q^2 = 0$ photoproduction. In terms of the underlying gluon distribution, the transition from the region of validity of the pQCD-improved parton model at $\eta(W^2, Q^2) > 1$ to the saturation region of $\eta(W^2, Q^2) < 1$ corresponds to a transition from (approximate) proportionality of the proton structure function to the gluon distribution to a logarithmic dependence on the gluon distribution function. Our specific ansatz for the dipole cross section that interpolates between the limits of $\eta(W^2, Q^2) \gg 1$ and $\eta(W^2, Q^2) \ll 1$ describes the experimental data for the proton structure function in the full range of $0.036 \leq Q^2 \leq 316 \text{ GeV}^2$.

Keywords: Deep inelastic scattering, dipole picture, low-x physics, saturation.

1. Introduction

As a starting point, I go back to the 60's of the last century. Photon-hadron interactions at that time were experimentally known only within a very restricted domain of the kinematic variables, the energy W and the virtuality of the photon, Q^2 . The theory was dominated by the vector-meson-dominance picture, see ref. [1] for a recent review. The real or virtual photon was conjectured to virtually dissociate, to “fluctuate” in mod-

ern jargon, into the vector mesons, ρ^0 , ω and ϕ . The subsequent interaction of ρ^0 , ω , and ϕ with a nucleon implied “hadronlike behavior” of photon-hadron interactions, well verified experimentally in e.g. vector meson production, the total photon-nucleon cross section and other reactions. The generalization from the scattering on nucleons to the scattering of photons on complex nuclei of high mass number implied hadronlike “shadowing” [2] as a consequence of the destructive interference of a one-step and a two-step reaction mechanism

within the nucleus. Shadowing in the interaction of real ($Q^2 = 0$) photons with complex nuclei was subsequently confirmed by experiments at DESY and SLAC.

The picture of photon-hadron interactions changed dramatically, when electron beams of much higher energy became available at the Stanford Linear Accelerator Center. The 1969 results of the SLAC-MIT collaboration on “deep inelastic scattering (DIS)” showed evidence for the scaling behavior that had been predicted by Bjorken, and they gave rise to Feynman’s interpretation of DIS in terms of the parton model.

An alternative interpretation of the DIS results from the SLAC-MIT collaboration, in particular in the diffraction region of low values of the Bjorken variable – of relevance in the present context as a starting point of the modern point of view of the color dipole picture (CDP) – was given by Sakurai and myself in 1972 [3].

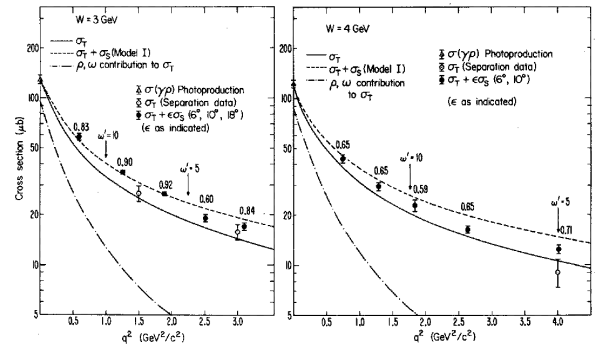


Figure 1: The SLAC-MIT experimental data compared with GVD predictions [3]

Volume 40B, number 1

PHYSICS LETTERS

12 June 1972

GENERALIZED VECTOR DOMINANCE
AND INELASTIC ELECTRON-PROTON SCATTERING *

J. J. SAKURAI and D. SCHILDKNECHT**
Department of Physics, University of California,
Los Angeles, USA

Received 30 March 1972

* We propose a model of inelastic electron-proton scattering which takes into account the coupling of the photon to higher-mass vector states. Both the virtual photon-proton cross section σ_T (predicted with essentially no adjustable parameters) and the q^2 dependence of R are in exceedingly good agreement with the SLAC-MIT data in the diffraction region.

In the generalized vector dominance (GVD) approach [3, 4] of 1972, it was conjectured that the slow decrease with increasing Q^2 of the photoabsorption cross section observed by the SLAC-MIT collaboration was due to so far unobserved couplings of the photon to a continuum of hadron states, more massive than the vector mesons, ρ^0, ω, ϕ . Compare Fig. 1 for the comparison of the successful GVD prediction with the DIS data from the SLAC-MIT collaboration.

The interpretation of the DIS data in terms of photon couplings to a high-mass continuum, $\gamma^* \rightarrow$ continuum states, in addition to the $\gamma^* \rightarrow \rho^0, \omega, \phi$ coupling required the persistence of shadowing, when real photons were replaced by virtual ones. In the 70’s and 80’s of last century, it was frequently argued that the GVD approach was invalid due to the lack of shadowing in the scattering of virtual photons on complex nuclei. After many years of confusion, in 1989 however, shadowing in the reaction of virtual photons with nuclei was discovered by the EMC collaboration [5]. The results are consistent with the theoretical prediction [6] from

GVD, compare Fig. 2.

Shadowing, being due to destructive interference between a one-step and a two-step process, for virtual photons, $Q^2 > 0$, requires the existence of diffractive production of states more massive than ρ^0, ω, ϕ . Accordingly, it came without surprise that immediately after the start of HERA, in 1994, the existence of high-mass diffractive production (“large-rapidity-gap events”) was established at HERA.

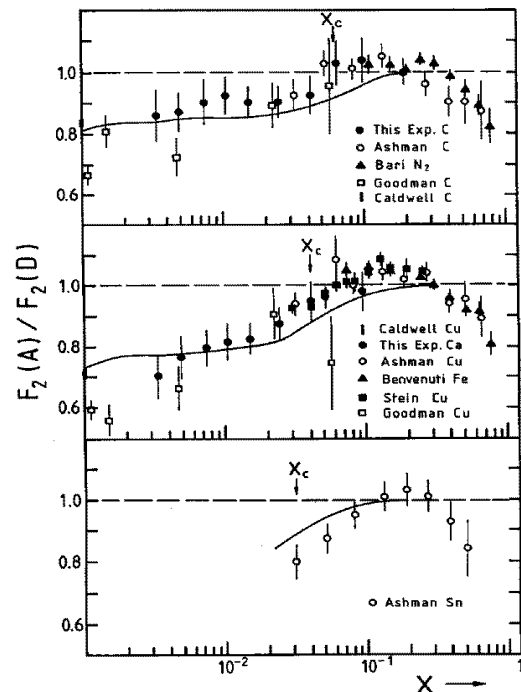


Figure 2: Shadowing in the scattering of virtual photons from complex nuclei compared with GVD predictions [6]

2. The modern picture of DIS at low x : the color dipole picture

As in GVD, in the modern approach, the photoabsorption reaction proceeds in two steps, i) the $\gamma^* \rightarrow q\bar{q}$ transition and ii) the $(q\bar{q})$ -proton interaction, whereby taking into account

- i) the internal structure of the $q\bar{q}$ system via the variable $0 \leq z \leq 1$ that specifies the longitudinal momentum distribution between the quark and the antiquark the photon fluctuates into, compare Fig. 3, and

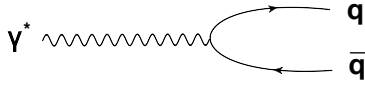


Figure 3: The $\gamma^* q\bar{q}$ transition.

- ii) the $q\bar{q}$ interaction with the gluon field in the nucleon [7] as a gauge-invariant color-dipole interaction, compare the (virtual) forward Compton scattering amplitude in Fig. 4.

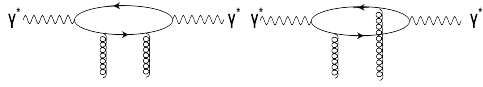


Figure 4: Two of the four diagrams for the $q\bar{q}$ dipole interaction with the gluon field in the nucleon

After Fourier transform to transverse position space, the photoabsorption cross section at low $x \simeq Q^2/W^2 < 0.1$ takes the form [8, 9]

$$\sigma_{\gamma_{L,T}^*}(W^2, Q^2) = \int dz \int d^2\vec{r}_\perp |\psi_{L,T}(\vec{r}_\perp, z(1-z), Q^2)|^2 \cdot \sigma_{(q\bar{q})p}(\vec{r}_\perp, z(1-z), W^2). \quad (2.1)$$

The quantity $|\psi_{L,T}(\vec{r}_\perp, z(1-z), Q^2)|^2$ may be interpreted as the probability for a longitudinally or a transversely polarized photon, $\gamma_{L,T}^*$, of virtuality Q^2 to undergo a transition to a $q\bar{q}$ state, $\gamma_{L,T}^* \rightarrow q\bar{q}$, being characterized by the transverse size \vec{r}_\perp and by the distribution of the longitudinal momenta of quark and antiquark determined by $z(1-z)$. In the rest frame of the $q\bar{q}$ fluctuation of mass $M_{q\bar{q}}$, the quantity $z(1-z)$ determines [9] the direction of the quark (antiquark) with respect to the photon direction. The interaction cross section of the $q\bar{q}$ dipole state in (2.1) is denoted by $\sigma_{(q\bar{q})p}(\vec{r}_\perp, z(1-z), W^2)$. It depends on the energy, W , [9, 10, 11, 12] of the $(q\bar{q})p$ interaction, since the photon fluctuates into an on-shell $q\bar{q}$ state of mass $M_{q\bar{q}}$ that subsequently interacts with

the nucleon. For generality, a dependence on $z(1-z)$ is allowed for in the dipole-proton cross section.

The gauge-invariant two-gluon interaction ii) of the $q\bar{q}$ dipole enters the photoabsorption cross section in (2.1) via [8, 9]

$$\sigma_{(q\bar{q})p}(\vec{r}_\perp, z(1-z), W^2) = \int d^2\vec{l}_\perp \bar{\sigma}(\vec{l}_\perp^2, z(1-z), W^2) \left(1 - e^{-i\vec{l}_\perp \cdot \vec{r}_\perp}\right). \quad (2.2)$$

In (2.2), \vec{l}_\perp stands for the transverse momentum of the absorbed gluon, and the first and the second term in the parenthesis on the right-hand side in (2.2), respectively, corresponds to the first and the second diagram in Fig. 2.

For the subsequent discussions, it will be useful to equivalently rewrite [13, 14] the photoabsorption cross section (2.1), in terms of dipole states, $(q\bar{q})_{L,T}^{J=1}$, that describe longitudinally and transversely polarized $q\bar{q}$ states of fixed spin $J = 1$ and polarization index L and T . In terms of the corresponding dipole cross section, $\sigma_{(q\bar{q})_{L,T}^{J=1}p}(\vec{r}'_\perp, W^2)$, where $\vec{r}'_\perp = \vec{r}_\perp z(1-z)$, the photoabsorption cross section (2.1) becomes [13, 14]

$$\sigma_{\gamma_{L,T}^*p}(W^2, Q^2) = \frac{\alpha}{\pi} \sum_q Q_q^2 Q^2 \int dr'_\perp{}^2 K_{0,1}^2(r'_\perp Q) \sigma_{(q\bar{q})_{L,T}^{J=1}p}(r'_\perp, W^2). \quad (2.3)$$

In the transition from (2.1) to (2.3), assuming massless quarks, we inserted the explicit expressions for $|\psi_{L,T}(\vec{r}_\perp, z(1-z), Q^2)|^2$ in terms of the modified Bessel functions $K_0(r'_\perp Q)$ and $K_1(r'_\perp Q)$, and Q stands for $Q \equiv \sqrt{Q^2}$. The sum over the squared charges of the actively contributing quarks is given by $\sum_q Q_q^2$, and the cross section $\sigma_{(q\bar{q})_{L,T}^{J=1}p}(r'_\perp, W^2)$ is related to the dipole cross section in (2.1) by an appropriate projection.

In terms of the $J = 1$ projection, $\sigma_{(q\bar{q})_{L,T}^{J=1}p}(r'_\perp, W^2)$, of the dipole cross section in (2.1), with $\vec{l}'_\perp{}^2 = \vec{l}_\perp^2/z(1-z)$, the two-gluon-coupling structure of the dipole cross section in (2.2) becomes

$$\sigma_{(q\bar{q})_{L,T}^{J=1}p}(r'_\perp, W^2) = \pi \int d\vec{l}'_\perp{}^2 \bar{\sigma}_{(q\bar{q})_{L,T}^{J=1}p}(\vec{l}'_\perp{}^2, W^2) \cdot \left(1 - \frac{\int d\vec{l}_\perp{}^2 \bar{\sigma}_{(q\bar{q})_{L,T}^{J=1}p}(\vec{l}_\perp{}^2, W^2) J_0(l'_\perp r'_\perp)}{\int d\vec{l}_\perp{}^2 \bar{\sigma}_{(q\bar{q})_{L,T}^{J=1}p}(\vec{l}_\perp{}^2, W^2)}\right), \quad (2.4)$$

where $J_0(l'_\perp r'_\perp)$ denotes the Bessel function with index 0.

Two distinct W -dependent limits of the dipole cross section (2.4) will be relevant [14] and important for

the ensuing discussions. We assume that the integrals in (2.4) exist and are determined by a W -dependent restricted range of $\vec{l}'^2 < \vec{l}'^2_{Max}(W^2)$, in which $\bar{\sigma}_{(q\bar{q})_{L,T}^{J=1}p}(\vec{l}'^2, W^2)$ is appreciably different from zero, $\vec{l}'^2_{Max}(W^2)$ increasing with increasing W^2 . The resulting cross section for a dipole of fixed transverse size, r'_\perp , strongly depends on the variation of the phase $l'_\perp r'_\perp$:

A) For

$$0 < l'_\perp r'_\perp < l'_{\perp Max}(W^2) r'_\perp \ll 1, \quad (2.5)$$

upon employing the expansion

$$J_0(l'_\perp r'_\perp) \cong 1 - \frac{1}{4}(l'_\perp r'_\perp)^2 + \frac{1}{4^3}(l'_\perp r'_\perp)^4 + \dots, \quad (2.6)$$

we find strong destructive interference between the two additive contributions to the $J = 1$ dipole cross section (2.4) which correspond to the first and the second diagram in Fig. 4. The dipole cross section (2.4) becomes proportional to r'^2_\perp (“color transparency” limit [8])

$$\sigma_{(q\bar{q})_{L,T}^{J=1}p}(r'^2_\perp, W^2) = \quad (2.7)$$

$$\frac{1}{4} r'^2_\perp \sigma_L^{(\infty)}(W^2) \Lambda_{sat}^2(W^2) \cdot \left\{ \begin{array}{l} 1, \\ \rho_W, \end{array} \right.$$

$$\left. \left(r'^2_\perp \ll \frac{1}{l'^2_{\perp Max}(W^2)} \right) \right\},$$

where by definition the W^2 -dependent scale $\Lambda_{sat}^2(W^2)$ reads

$$\Lambda_{sat}^2(W^2) \equiv \frac{1}{\sigma_L^{(\infty)}(W^2)} \pi \cdot \int d\vec{l}'^2_{\perp} d\vec{l}''^2_{\perp} \bar{\sigma}_{(q\bar{q})_{L,T}^{J=1}p}(\vec{l}'^2_{\perp}, W^2), \quad (2.8)$$

and $\sigma_L^{(\infty)}(W^2)$ is explicitly defined by (2.11) below. For vanishing size, \vec{r}'^2_\perp , the $q\bar{q}$ color dipole (obviously) has a vanishing cross section. The expression for the factor ρ_W in (2.7) is explicitly obtained by comparison of (2.7) with (2.4). According to (2.7), and anticipating $\rho_W > 1$, transversely polarized $(q\bar{q})^{J=1}$ states interact with enhanced transverse size [15, 14]

$$\vec{r}'^2_\perp \rightarrow \rho_W \vec{r}'^2_\perp \quad (2.9)$$

relative to longitudinal ones. The ratio ρ_W will be shown to be a W -independent constant of definite magnitude, $\rho_W = \rho = 4/3$.

B) For the case of

$$l'_{\perp Max}(W^2) r'_\perp \gg 1, \quad (2.10)$$

alternative to (2.5), for any fixed value of r'_\perp , rapid oscillations of the Bessel function in (2.4) lead to a vanishingly small contribution of the second term in (2.4) thus implying (“saturation” limit)

$$\sigma_{(q\bar{q})_{L,T}^{J=1}p}(r'^2_\perp, W^2) \cong \pi \int d\vec{l}'^2_{\perp} \bar{\sigma}_{(q\bar{q})_{L,T}^{J=1}p}(\vec{l}'^2_{\perp}, W^2) \equiv \sigma_{L,T}^{(\infty)}(W^2), \quad \left(r'^2_\perp \gg \frac{1}{l'^2_{\perp Max}(W^2)} \right). \quad (2.11)$$

The high-energy limit in (2.11) of sufficiently large W at fixed dipole size r'_\perp , according to (2.4), coincides with the limit of sufficiently large r'_\perp at fixed W , i.e.

$$\lim_{\substack{r'^2_\perp \rightarrow \infty \\ W = \text{const}}} \sigma_{(q\bar{q})_{L,T}^{J=1}p}(r'^2_\perp, W^2) = \sigma_{L,T}^{(\infty)}(W^2). \quad (2.12)$$

At fixed dipole size, with sufficiently large energy, we arrive at the large-dipole-size limit of the (at most weakly W -dependent) hadronic cross section $\sigma_{L,T}^{(\infty)}(W^2) \simeq \sigma^{(\infty)}$.

The photoabsorption cross section in (2.3), due to the strong decrease of the modified Bessel functions $K_{0,1}(r'_\perp Q)$ with increasing argument $r'_\perp Q$, is strongly dominated and actually determined at any fixed value of Q^2 by values of r'^2_\perp such that $r'^2_\perp Q^2 < 1$. Whether color transparency of the dipole cross section according to (2.5) and (2.7) or, alternatively, saturation according to (2.10) and (2.11) is relevant for $\sigma_{\gamma^*p}(W^2, Q^2)$ in (2.3) depends on whether $Q^2 \gg \Lambda_{sat}^2(W^2)$ or $Q^2 \ll \Lambda_{sat}^2(W^2)$ is realized at a specific value of W . Upon substitution of (2.7) and, alternatively, of (2.11) into (2.3), for $\sigma_{\gamma^*p}(W^2, Q^2) = \sigma_{\gamma^*p}(W^2, Q^2) + \sigma_{\gamma^*p}(W^2, Q^2)$ one finds [10, 14]

$$\sigma_{\gamma^*p}(W^2, Q^2) = \sigma_{\gamma^*p}(\eta(W^2, Q^2)) = \frac{\alpha}{\pi} \sum_q Q_q^2 \quad (2.13)$$

$$\cdot \begin{cases} \frac{1}{6}(1 + 2\rho)\sigma^{(\infty)} \frac{1}{\eta(W^2, Q^2)}, & (\eta(W^2, Q^2) \gg 1), \\ \sigma^{(\infty)} \ln \frac{1}{\eta(W^2, Q^2)}, & (\eta(W^2, Q^2) \ll 1), \end{cases}$$

where we have introduced the low- x scaling variable

$$\eta(W^2, Q^2) = \frac{Q^2 + m_0^2}{\Lambda_{sat}^2(W^2)}, \quad (2.14)$$

and anticipated $\rho_W = \text{const.} = \rho$. In (2.14), via quark-hadron duality [3, 16], we introduced the lower bound

$m_0^2 \lesssim m_p^2$ on the masses of the $q\bar{q}$ fluctuations $M_{q\bar{q}}^2 \geq m_0^2$, only relevant in the limit of $Q^2 \rightarrow 0$.

From the above derivation, leading to (2.13), it has become clear that DIS at low x proceeds via two different reaction channels. They correspond to the first and the second diagram in Fig. 4. For sufficiently large $Q^2 \gg \Lambda_{sat}^2(W^2)$ both channels are open, resulting in strong destructive interference between them. With decreasing Q^2 at fixed W , or with increasing W at fixed Q^2 , for $Q^2 \ll \Lambda_{sat}^2(W^2)$, the second channel becomes closed, no destructive interference any more. Only the first channel remains open, implying that the proportionality of the photoabsorption cross section to $\Lambda_{sat}^2(W^2)$ turns into the (soft) energy dependence proportional to $\ln \Lambda_{sat}^2(W^2)$, compare (2.13).

The longitudinal-to-transverse ratio of the photoabsorption cross sections $\sigma_{\gamma_L^* p}(W^2, Q^2)$ and $\sigma_{\gamma_T^* p}(W^2, Q^2)$ at large $Q^2 \gg \Lambda_{sat}^2(W^2)$ according to (2.13) is given by

$$R(W^2, Q^2)_{Q^2 \gg \Lambda_{sat}^2(W^2)} = \frac{\sigma_{\gamma_L^* p}(W^2, Q^2)}{\sigma_{\gamma_T^* p}(W^2, Q^2)} \Big|_{Q^2 \gg \Lambda_{sat}^2(W^2)} = \frac{1}{2\rho}. \quad (2.15)$$

The factor 2 in (2.15) originates from the difference in the photon wave functions in (2.3). The interaction with enhanced transverse size of $(q\bar{q})_T^{J=1}$ states relative to $(q\bar{q})_L^{J=1}$ states, ρ_W in (2.9), is a consequence of the ratio of the average transverse momenta of the quark (antiquark) in the $(q\bar{q})_T^{J=1}$ state relative to the quark (antiquark) in the $(q\bar{q})_L^{J=1}$ state. Upon applying the uncertainty principle, one obtains [15, 14]

$$\rho_W = \rho = \frac{4}{3}. \quad (2.16)$$

The longitudinal structure function, with (2.15) and (2.16), at large Q^2 is related to the transverse one via

$$F_L(x, Q^2) = \frac{1}{1+2\rho} F_2(x, Q^2) = 0.27 F_2(x, Q^2). \quad (2.17)$$

The result is consistent with the experimental data (compare Fig. 5).

The W -dependence in (2.1) and (2.3) of the dipole cross section, combined with the $1/Q^2$ dependence in (2.13) at large Q^2 , implies that the structure function $F_2(x, Q^2) \simeq (Q^2/4\pi^2\alpha)(\sigma_{\gamma_L^* p}(W^2, Q^2) + \sigma_{\gamma_T^* p}(W^2, Q^2))$ becomes a function of the single variable W^2 . The experimental data in Fig. 6, in the relevant range of $x \simeq Q^2/W^2 < 0.1$, approximately corresponding to $1/W^2 \leq 10^{-3}$, indeed show the expected tendency to lie on a single line [14]. An eye-ball fit to the data in

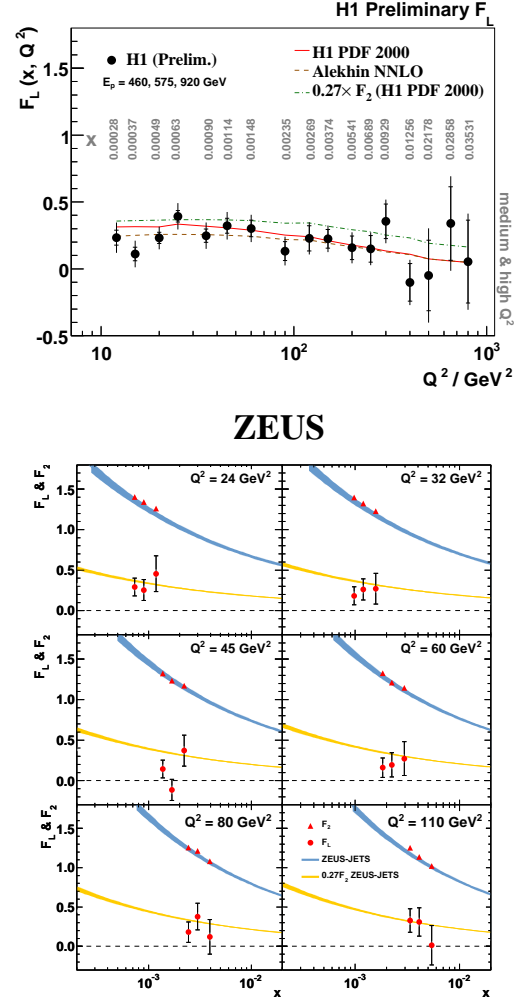


Figure 5: The prediction (2.17) compared with the experimental data for F_L and F_2 .

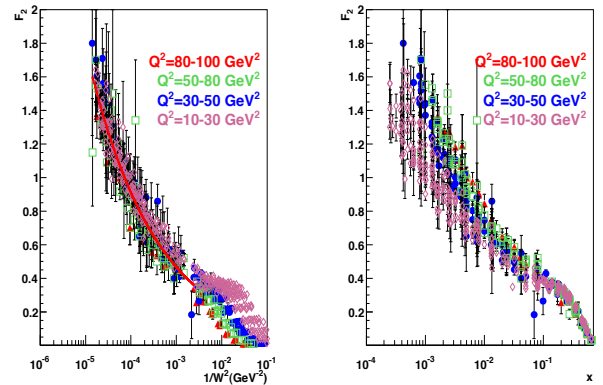


Figure 6: The structure function $F_2(x, Q^2)$ as a function of $1/W^2$ and as a function of x

Fig. 6¹ yields

$$F_2(W^2) = f_2 \cdot \left(\frac{W^2}{1 \text{ GeV}^2} \right)^{C_2=0.29} \quad (2.18)$$

with $f_2 = 0.063$. We will come back to representation (2.18) of $F_2(W^2)$ below. For comparison, in Fig. 6, we also show $F_2(x, Q^2)$ as a function of x .

In Fig. 7, we show experimental evidence for the low- x scaling behavior, $\sigma_{\gamma^*p}(W^2, Q^2) = \sigma_{\gamma^*p}(\eta(W^2, Q^2))$ of (2.13), with $\eta(W^2, Q^2)$ from (2.14), first obtained in ref. [10] by a model-independent analysis. The experimental data confirm this general prediction of the CDP of scaling in $\eta(W^2, Q^2)$ in the form (2.13), which is independent of any specific ansatz for the dipole cross section. The theoretical curve in Fig. 7 is due to the ansatz [10, 14] for the dipole cross section to be discussed in Section 4.

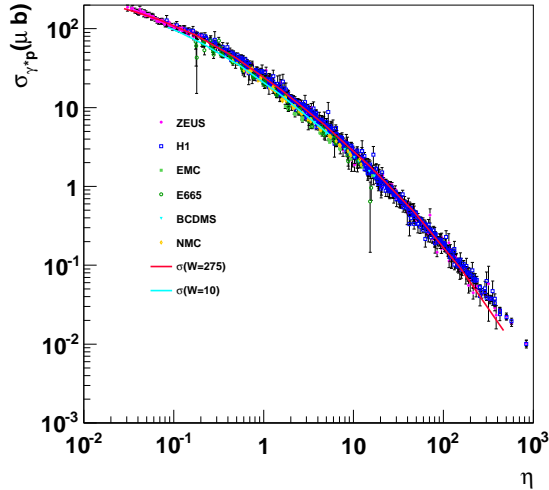


Figure 7: Scaling of $\sigma_{\gamma^*p}(W^2, Q^2) = \sigma_{\gamma^*p}(\eta(W^2, Q^2))$.

The logarithmic dependence of the photoabsorption cross section in (2.13), for $W^2 \rightarrow \infty$ at fixed Q^2 leads to [17]

$$\lim_{\substack{W^2 \rightarrow \infty \\ Q^2 \text{ fixed}}} \frac{\sigma_{\gamma^*p}(\eta(W^2, Q^2))}{\sigma_{\gamma^*p}(\eta(W^2, Q^2 = 0))} = \lim_{\substack{W^2 \rightarrow \infty \\ Q^2 \text{ fixed}}} \frac{\ln \left(\frac{\Lambda_{sat}^2(W^2)}{m_0^2} \frac{m_0^2}{(Q^2 + m_0^2)} \right)}{\ln \frac{\Lambda_{sat}^2(W^2)}{m_0^2}} = 1 + \lim_{\substack{W^2 \rightarrow \infty \\ Q^2 \text{ fixed}}} \frac{\ln \frac{m_0^2}{Q^2 + m_0^2}}{\ln \frac{\Lambda_{sat}^2(W^2)}{m_0^2}} = 1. \quad (2.19)$$

¹The representation of the experimental data in Fig. 6 was kindly provided by Prabhdeep Kaur Devgun.

In this limit of (2.19), the photoabsorption cross section tends to a Q^2 -independent limit that coincides with $Q^2 = 0$ photoproduction. The convergence to this limit is extremely slow. Compare Fig. 8, where this limit is seen in terms of the structure function $F_2(x, Q^2)$,

$$\lim_{\substack{W^2 \rightarrow \infty \\ Q^2 \text{ fixed}}} \frac{F_2(x \cong Q^2/W^2, Q^2)}{\sigma_{\gamma p}(W^2)} = \frac{Q^2}{4\pi^2\alpha}. \quad (2.20)$$

The theoretical curve in Fig. 8 is due to the concrete ansatz for the dipole cross section in Section 4 that interpolates between the regions of $\eta(W^2, Q^2) \gg 1$ and $\eta(W^2, Q^2) \ll 1$.

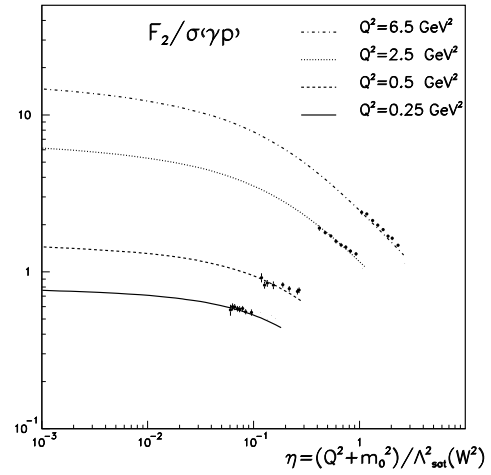


Figure 8: The approach to saturation.

An approach to a Q^2 -independent limit for $W^2 \rightarrow \infty$ at fixed Q^2 was recently independently observed by Caldwell[18] based on a purely empirical fit to the experimental data given by

$$\sigma_{\gamma^*p}(W^2, Q^2) = \sigma_0(Q^2) \left(\frac{1}{2M_p} \frac{W^2}{Q^2} \right)^{\lambda_{eff}(Q^2)}. \quad (2.21)$$

The straight lines in Fig. 9 meet at a value of W^2 approximately given by $W^2 \simeq 10^9 Q^2$, consistent with the above conclusion from the CDP.

The results from the above general analysis of the CDP lead to the simple structure of the (Q^2, W^2) plane shown in Fig. 10. The (Q^2, W^2) plane is subdivided into only two regions as a consequence of the two interaction channels corresponding to the diagrams in Fig. 4. For $\eta(W^2, Q^2) > 1$, both interaction channels, channels 1 and 2, are open, implying color transparency of the $(q\bar{q})p$ dipole interaction with strong destructive interference. For $\eta(W^2, Q^2) \ll 1$, channel 2 becomes closed. The lack of destructive interference leads to a saturation

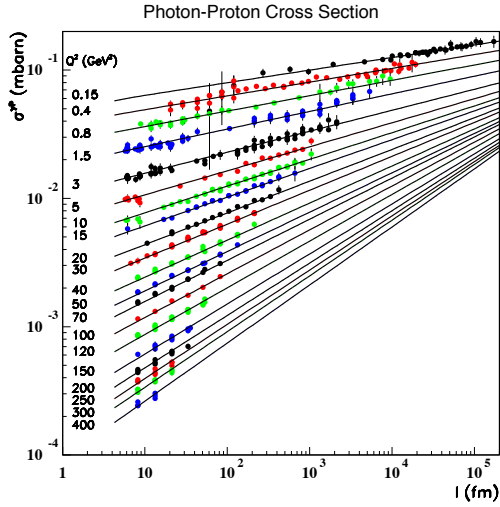
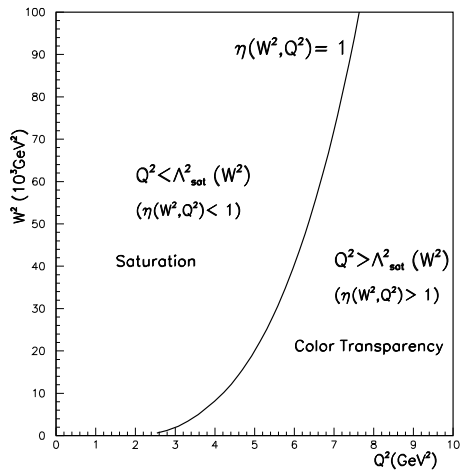


Figure 9: The Caldwell fit (2.21) [18].

Figure 10: The Q^2, W^2 plane of the CDP. The line $\eta(W^2, Q^2) = 1$ subdivides the (Q^2, W^2) plane into the saturation region of $\eta(W^2, Q^2) < 1$ and the color transparency region of $\eta(W^2, Q^2) > 1$.

of the cross section determined by the dipole interaction solely via channel 1. The virtual-photon-nucleon cross section approaches a Q^2 -independent saturation limit that coincides with $Q^2 = 0$ photoproduction.

3. The CDP, the gluon distribution function and evolution

The CDP of DIS corresponds² to the low x approximation of the pQCD-improved parton model in which

²With respect to this Section, compare also ref. [19]

the interaction of the (virtual) photon occurs by interaction with the quark-antiquark sea in the proton via $\gamma^* \text{gluon} \rightarrow q\bar{q}$ fusion.

The longitudinal structure function in this approximation, for a wide range of different gluon distributions, becomes proportional to the gluon density at a rescaled value x/ξ_L [20]

$$F_L(\xi_L x, Q^2) = \frac{\alpha_s(Q^2)}{3\pi} \sum_q Q_q^2 G(x, Q^2), \quad (3.1)$$

where $G(x, Q^2) \equiv xg(x, Q^2)$ and $g(x, Q^2)$ stands for the gluon distribution function. The rescaling factor has the preferred value of $\xi_L \simeq 0.40$.

The structure function $F_2(x, Q^2)$ at low x in this approximation is proportional to the sea-quark distribution, and again for a wide range of different gluon distributions, the evolution of the structure function $F_2(x, Q^2)$ with Q^2 is determined by [21, 22]

$$\frac{\partial F_2(\xi_2 x, Q^2)}{\partial \ln Q^2} = \frac{\alpha_s(Q^2)}{3\pi} \sum_q Q_q^2 G(x, Q^2), \quad (3.2)$$

where the preferred value of ξ_2 is given by $\xi_2 \simeq 0.50$.

According to the CDP, compare (2.13), and supported by the experimental data in Fig. 6, the structure function $F_2(x, Q^2)$ for sufficiently large Q^2 becomes a function of the single variable W^2 ,

$$F_2(x, Q^2) = F_2(W^2 = \frac{Q^2}{x}). \quad (3.3)$$

Employing the proportionality of $F_L(x, Q^2) = (1/(1 + 2\rho_W))F_2(x, Q^2)$ from (2.7) and (2.17), and combining (3.1) and (3.2), upon inserting (3.3) the evolution equation becomes

$$(2\rho_W + 1) \frac{\partial}{\partial \ln W^2} F_2\left(\frac{\xi_L}{\xi_2} W^2\right) = F_2(W^2). \quad (3.4)$$

A potential dependence of ρ_W on the energy W is allowed in (3.4).

We specify $F_2(W^2)$ by adopting the power law [14]

$$F_2(W^2) \sim (W^2)^{C_2} = \left(\frac{Q^2}{x}\right)^{C_2}. \quad (3.5)$$

A power law in $(1/x)^\lambda$ with λ occurs e.g. in the ‘‘hard Pomeron solution’’ [23] of DGLAP evolution as well as in the ‘‘hard Pomeron’’ part of Regge phenomenology with $(1/x)^{\epsilon_0}$ and $\epsilon_0 \simeq 0.43$ from a fit [24]. The CDP in (3.5) is more specific, however, since the W dependence of $F_2(W^2)$ implies that the x dependence and the Q^2 dependence are intimately related to each other.

Substitution of (3.5) into (3.4) implies the constraint [14]

$$(2\rho_W + 1)C_2 \left(\frac{\xi_L}{\xi_2} \right)^{C_2} = 1. \quad (3.6)$$

If, and only if $\rho_W = \rho = \text{const.}$, also the exponent is constant, $C_2 = \text{const.}$ With the CDP result of $\rho = 4/3$ from (2.16), we obtain the unique value of

$$C_2 = \frac{1}{2\rho + 1} \left(\frac{\xi_2}{\xi_L} \right)^{C_2} = 0.29, \quad (3.7)$$

where $\rho = 4/3$ and $\xi_2/\xi_L = 1.25$ was inserted. The result for $C_2 = 0.29$ is fairly insensitive under variation of ξ_2/ξ_L . For $1 \leq \xi_2/\xi_L \leq 1.5$, one obtains $0.27 \leq C_2 \leq 0.31$. The value of $C_2 = 0.29$ is consistent with the experimental data, compare (2.18) and Fig. 6.

Imposing consistency between the CDP and the pQCD-improved parton model, we thus arrived at the prediction of a definite value of $C_2 = 0.29$ that coincides with the experimental findings in Fig. 6.

The underlying gluon distribution function can now be deduced from (3.1) by expressing the longitudinal structure function in terms of $F_2(x, Q^2)$ according to (2.17) and inserting the power law (2.18),

$$\alpha_s(Q^2)G(x, Q^2) = \frac{3\pi}{\sum_q Q_q^2(2\rho + 1)} \frac{f_2}{\xi_L^{C_2=0.29}} \left(\frac{W^2}{1\text{GeV}^2} \right)^{C_2=0.29}. \quad (3.8)$$

With $\rho = 4/3$ from the CDP, compare (2.16), the result (3.8) contains the single free fitted parameter $f_2 = 0.063$ from (2.18). Inserting $W^2 = Q^2/x$, from (3.8), we obtain the gluon distribution as a function of x and Q^2 .

Using the next-to-leading order expression for $\alpha_s(Q^2)$, in Fig. 11 [14], we compare the gluon distribution (3.8) with various gluon distributions obtained in sophisticated fits to the experimental data. The consistency of our simple one-free-parameter extraction of the gluon distribution from Fig. 6 according to (3.8) may indicate that the gluon distribution is less sensitively dependent on the details of the $ggpp$ structure than usually assumed, or elaborated upon and employed in the global fits to the experimental data.

4. Specific ansatz for the dipole cross section and comparison with experiment

Any specific ansatz for the dipole cross section has to interpolate between the region of $\eta(W^2, Q^2) \gg 1$, where $\sigma_{\gamma^*p}(\eta(W^2, Q^2)) \sim 1/\eta(W^2, Q^2)$, and the region of $\eta(W^2, Q^2) \ll 1$, where $\sigma_{\gamma^*p}(\eta(W^2, Q^2)) \sim$

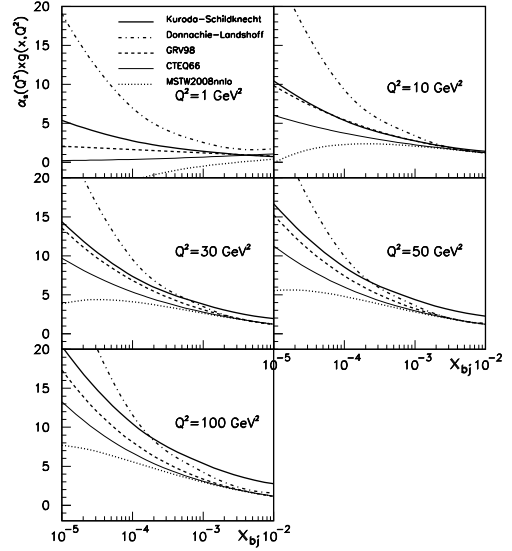


Figure 11: The gluon distribution function (3.8) compared with the results from the hard Pomeron part of a Regge fit to $F_2(x, Q^2)$ and from the fits GRV [25] CTEQ [26] and [27].

$\ln(1/\eta(W^2, Q^2))$, compare (2.13). For the explicit expressions for the ansatz for the dipole cross section, we refer to refs. [10] and [14]. We only note that the saturation scale, $\Lambda_{sat}^2(W^2) \sim (W^2)^{C_2}$ in the HERA energy range approximately varies between $2 \leq \Lambda_{sat}^2(W^2) \leq 7 \text{ GeV}^2$, and restrict ourselves to presenting a comparison with the experimental data. The theoretical results from the CDP in Figs. 12 and 13 show agreement with

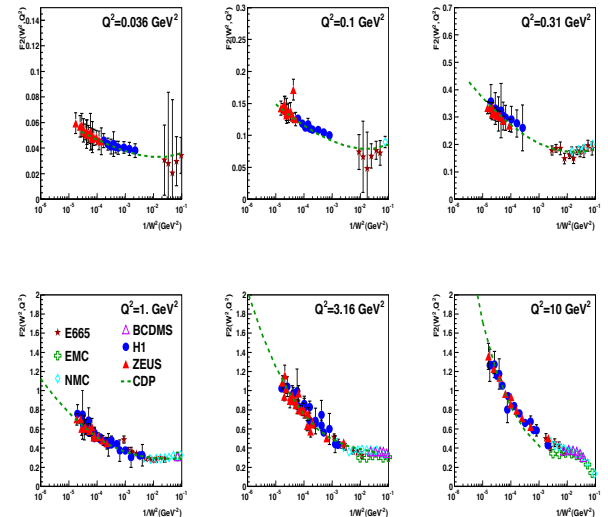
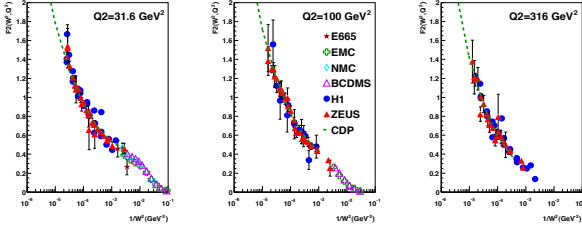


Figure 12: The predictions [14] from the CDP for the structure function $F_2(W^2, Q^2)$ compared with the experimental data for $0.036 \leq Q^2 \leq 10 \text{ GeV}^2$.

Figure 13: As in Fig. 12, but for $31.6 \leq Q^2 \leq 316 \text{ GeV}^2$.

the experimental data³ for $F_2(W^2, Q^2)$ over the full relevant region of $0.036 \leq Q^2 \leq 316 \text{ GeV}^2$.

In Figs. 14 and 15, in addition to the theoretical results from the CDP, we also show, for comparison, the results from the pQCD improved parton model based on the gluon distribution function (3.8) shown in Fig. 11.

Explicitly, by returning to (2.18) and inverting (3.8), we reinterpret (3.8) as a prediction from the (previously determined) gluon distribution according to

$$F_2(W^2 = Q^2/x) = f_2 \left(\frac{W^2}{1 \text{ GeV}^2} \right)^{C_2=0.29} = \frac{(2\rho + 1) \sum_q Q_q^2}{3\pi} \xi_L^{C_2=0.29} \alpha_s(Q^2) G(x, Q^2), \quad (4.1)$$

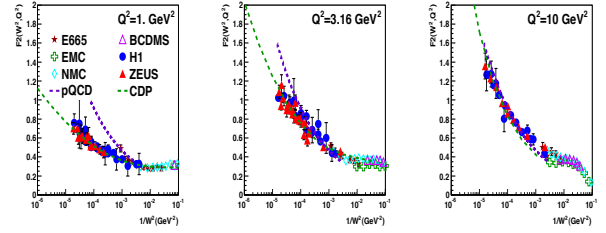
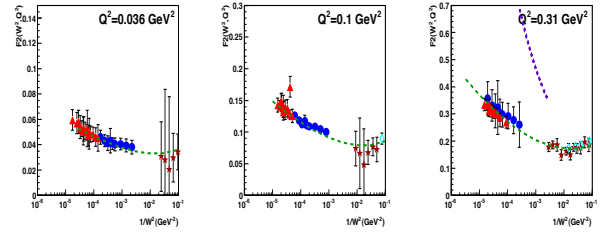
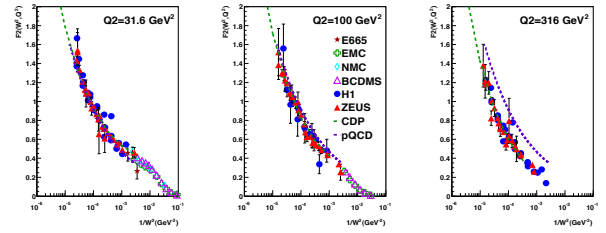
where $f_2 = 0.063$ and $\xi_L = 0.40$. In Figs. 14 and 15, we see the expected consistency of the pQCD prediction (4.1) with the experimental data and the CDP in the relevant range of $10 \leq Q^2 \leq 100 \text{ GeV}^2$. For $Q^2 < 10 \text{ GeV}^2$, with increasing W , gradually saturation sets in implying a breakdown of the pQCD proportionality (4.1) of the proton structure function to the gluon distribution.

The pQCD prediction for $Q^2 = 316 \text{ GeV}^2$ lies above the experimental data. This is due to the breakdown of the simple form for $F_2(W^2)$ in (2.18) which is used to extract the gluon distribution. Employing the full CDP result would lead to an appropriate decrease of the gluon distribution with increasing Q^2 for $Q^2 > 100 \text{ GeV}^2$.

The proton structure function of the CDP, according to (2.13), in the region of $\eta(W^2, Q^2) < 1$, starts to depend logarithmically on the saturation scale, $\Lambda_{sat}^2(W^2) \sim (W^2)^{C_2}$, and with $\alpha_s(Q^2)G(x, Q^2) \sim (W^2)^{C_2}$ from (3.8) and (4.1), it depends logarithmically on the gluon distribution,

$$F_2(W^2, Q^2) \sim Q^2 \sigma_L^{(\infty)} \ln \frac{\Lambda_{sat}^2(W^2 = Q^2/x)}{Q^2 + m_0^2}$$

³We thank Prabhdeep Kaur Devgun for providing the plots of the experimental data in Figs. 12 to 15.

Figure 14: In addition to the prediction from the CDP, also the pQCD prediction (4.1) based on the gluon distribution (3.8) is compared with the experimental data for $F_2(W^2, Q^2)$.Figure 15: As in Fig. 14, but for $31.6 \leq Q^2 \leq 316 \text{ GeV}^2$.

$$\sim Q^2 \sigma_L^{(\infty)} \ln \frac{\alpha_s(Q^2)G(x, Q^2)}{\sigma_L^{(\infty)}(Q^2 + m_0^2)}, \quad (Q^2 \ll \Lambda_{sat}^2(W^2)). \quad (4.2)$$

The smooth transition from the color transparency region to the saturation region does not correspond to a change in the W -dependent gluon distribution, $\alpha_s(Q^2)G(x, Q^2)$, but occurs via transition from the proportionality (4.1) to the logarithmic dependence (4.2) on the gluon distribution function. It is the same gluon distribution that is relevant in the region of color transparency $\eta(W^2, Q^2) \gg 1$ and in the saturation region, $\eta(W^2, Q^2) \ll 1$, but the functional dependence on the gluon distribution has changed. We disagree with the frequently expressed opinion (compare e.g. ref. [28] and the list of references given therein) that the mere existence of the saturation scale and of scaling like in Fig. 7 suggests and even requires a modification based on non-linear evolution of the gluon distribution determined in the pQCD domain of $\eta(W^2, Q^2) > 1$, when passing to the saturation region of $\eta(W^2, Q^2) < 1$.

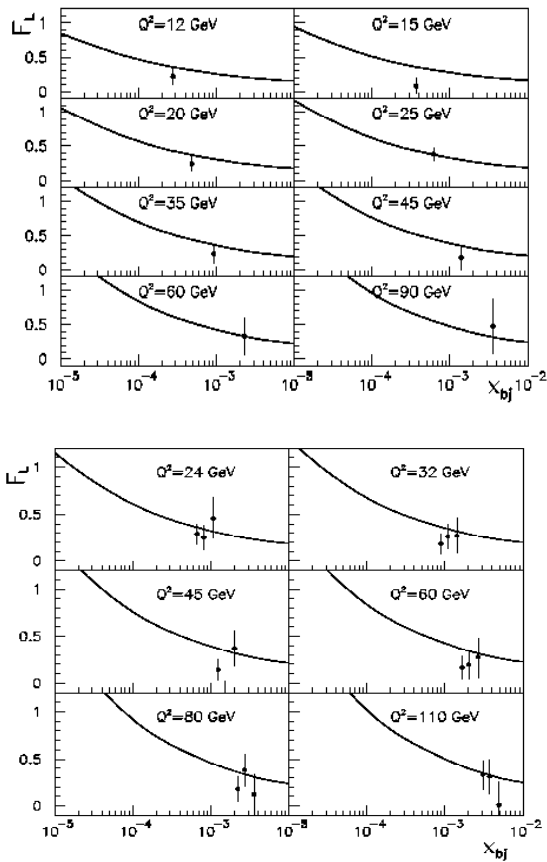


Figure 16: The longitudinal proton structure function $F_L(x, Q^2)$ from the H1 collaboration [29] and from the ZEUS collaboration [30] compared with the CDP prediction.

In Fig. 16, we show the longitudinal structure function, $F_L(x, Q^2)$, in comparison with the predictions from the CDP based on the specific ansatz for the dipole cross section that was used in Figs. 12 to 15.

5. Conclusions

The color-gauge-invariant dipole interaction with the nucleon in terms of the forward scattering amplitude proceeds via two reaction channels. They correspond to the two diagrams of Fig. 4. For a given dipole size, if both channels are open, the destructive interference between them implies color transparency. In the limit in which the reaction channel corresponding to the second diagram in Fig. 4 is closed, the dipole cross section saturates to a cross section of standard hadronic size with at most a weak energy dependence.

In the photoabsorption cross section, the above limits of color transparency and saturation are realized, respectively, by the two regions in the (Q^2, W^2) plane corresponding to $\eta(W^2, Q^2) \gg 1$ and $\eta(W^2, Q^2) \ll 1$. The (Q^2, W^2) plane (under the restriction of $Q^2/W^2 \lesssim 0.1$) is accordingly simple. There are only two distinct regions, separated by the line $\eta(W^2, Q^2) = 1$.

The main features of the experimental data on DIS at low x have thus been recognized to follow from the color-gauge-invariant dipole-proton interaction without adopting a specific ansatz for the dipole cross section. Any specific ansatz has to interpolate between the model-independent restrictions on the photoabsorption cross section that hold for $\eta(W^2, Q^2) \gg 1$ and for $\eta(W^2, Q^2) \ll 1$, respectively.

Acknowledgement

The author is grateful to Kuroda-san for a fruitful collaboration on the color dipole picture. Thanks to Prabhdeep Kaur Devgun for providing plots of experimental data. The author thanks Allen Caldwell and Reinhart Kögerler for useful discussions.

The lively scientific and pleasant atmosphere at Ringberg Castle is gratefully acknowledged.

References

- [1] D. Schildknecht, Acta Phys. Polon. B 37 (2006) 595 [hep-ph/0511090].
- [2] L. Stodolsky, Phys. Rev. Lett. 18 (1967) 135.
- [3] J.J. Sakurai, D. Schildknecht, Phys. Lett. B 40 (1972) 121; B. Gorczyca, D. Schildknecht, Phys. Lett. B 47 (1973) 71.
- [4] H. Fraas, B.J. Read, D. Schildknecht, Nucl. Phys. B 86 (1975) 346; R. Devenish, D. Schildknecht, Phys. Rev. D 19 (1976) 93.
- [5] EMC-NMC Collaboration, compare: M. Arneodo, Phys. Rept. 240 (1994) 301.
- [6] D. Schildknecht, Nucl. Phys. B 66 (1973) 398; C. Bilchak, D. Schildknecht, Phys. Lett. B 214 (1988) 441, Phys. Lett. B 233 (1989) 461.
- [7] F.E. Low, Phys. Rev. D 12 (1975) 163; S. Nussinov, Phys. Rev. Lett. 34 (1975) 1286, Phys. Rev. D 14 (1976) 246; J. Gunion, D. Soper, Phys. Rev. D 15 (1977) 2617.
- [8] N.N. Nikolaev, B.G. Zakharov, Z. Phys. C 49 (1991) 607.
- [9] G. Cvetic, D. Schildknecht, A. Shoshi, Eur. Phys. J. C 13 (2000) 301.
- [10] D. Schildknecht, Contribution to Diffraction 2000, Cetraro, Italy, September 2-7, 2000, Nucl. Phys. B, Proc. Supplement 99 (2001) 121; D. Schildknecht, B. Surrow, M. Tentyukov, Phys. Lett. B 499 (2001) 116; G. Cvetic, D. Schildknecht, B. Surrow, M. Tentyukov, Eur. Phys. J. C 20 (2001) 77.
- [11] J.R. Forshaw, G. Kerley, G. Shaw, Phys. Rev. D 60 (1999) 074012.

- [12] C. Ewerz, O. Nachtmann, *Annals Phys.* 322 (2007) 1635; 322 (2007) 1670;
C. Ewerz, A.v. Manteuffel, O. Nachtmann, *JHEP* 1103 (2011) 062 [arXiv:1101.0288 [hep-ph]].
- [13] M. Kuroda, D. Schildknecht, *Phys. Rev. D* 66 (2002) 094005; *Phys. Rev. D* 67 (2003) 094008.
- [14] M. Kuroda, D. Schildknecht, arXiv:1108.2584 [hep-ph].
- [15] M. Kuroda, D. Schildknecht, *Phys. Lett. B* 670 (2008) 129.
- [16] D. Schildknecht, F. Steiner, *Phys. Lett. B* 56 (1975) 36.
- [17] D. Schildknecht, Contribution to DIS 2001, The 9th Int. Workshop on Deep Inelastic Scattering, Bologna, Italy, 2001, G. Brassi *et al.* (Eds.), World Scientific, Singapore, 2002, p. 798; D. Schildknecht, B. Surrow, M. Tentyukov, *Mod. Phys. Lett. A* 16 (2001) 1829.
- [18] A. Caldwell, arXiv:0802.0769 [hep-ph].
- [19] D. Schildknecht, arXiv:1104.0850 [hep-ph]
- [20] A.D. Martin, R.G. Roberts, W.J. Stirling, *Phys. Rev. D* 37 (1988) 1161;
A.M. Cooper-Sarkar *et al.*, *Z. Phys. C* 39 (1988) 281.
- [21] L.N. Lipatov, *Sov. J. Nucl. Phys.* 20 (1975) 94;
V.N. Gribov, L.N. Lipatov, *Sov. J. Nucl. Phys.* 15 (1972) 438;
G. Altarelli, G. Parisi, *Nucl. Phys. B* 126 (1977) 298;
Yu.L. Dokshitzer, *Sov. Phys. JETP* 46 (1977) 641
- [22] K. Prytz, *Phys. Lett. B* 311 (1993) 286.
- [23] K. Adel, F. Barreiro, F.J. Yndurain, *Nucl. Phys. B* 495 (1997) 221;
F.J. Yndurain, *The Theory of Quark and Gluon Interactions*, Berlin, Germany: Springer (1999), p.157.
- [24] A. Donnachie, P.V. Landshoff, *Phys. Lett. B* 533 (2002) 277, [hep-ph/0111427]; *Acta Physica Polonica B* 34 (2003) 2989, [hep-ph/0305171].
- [25] M. Glück, E. Reya, A. Vogt, *Z. Phys. C* 67 (1995) 433; *Eur. Phys. J. C* 5 (1998) 461 [hep-ph/9806404].
- [26] CTEQ Collaboration: J. Pumplin *et al.*, *JHEP* 0207 (2002) 012.
- [27] A.D. Martin *et al.*, *Eur. Phys. J. C* 18 (2000) 117.
- [28] J. Kuokkanen, K. Rummukainen, H. Weigert, arXiv:1108.1867 [hep-ph].
- [29] H1 Collaboration, F.D. Aaron *et al.*, *Phys. Lett. B* 665 (2008) 139.
- [30] ZEUS Collaboration, S. Chekanov *et al.*, *Phys. Lett. B* 682 (2009) 8.